UNDRAINED LIMIT ANALYSES FOR COMBINED LOADING OF STRIP FOOTINGS ON CLAY

By Boonchai Ukritchon,[1] Andrew J. Whittle,[2] Member, ASCE, and Scott W. Sloan[3]

ABSTRACT: This paper applies numerical limit analyses to evaluate the undrained stability of surface footings on nonhomogeneous and layered clay deposits under the combined effects of vertical, horizontal, and moment (V, H, M) loading. The analyses are able to resolve the true collapse loads to within ±5% by computing rigorous upper and lower bound solutions for these plane strain problems using linear programming methods and finite element discretization. The results focus on the geometry of the three-dimensional failure envelope and illustrate the effects of underbase suction and non-homogeneous undrained strength profiles. The existing empirical bearing capacity factors for inclined, eccentric loading are conservative, often underestimating the exact collapse solutions for footings on homogeneous clay by more than 25%. However, the same correction factors can become completely unreliable when there is a significant undrained strength gradient. The numerically-derived failure envelope for footings on homogeneous clay is described approximately by curve fitting techniques using relatively simple functions that can be used to update the existing bearing capacity factors.

INTRODUCTION

The undrained stability of a shallow foundation on clay is conventionally computed using the bearing capacity equation of Terzaghi (1943). The core of this equation is the slip line solution of Prandtl (1920) for a vertically loaded surface strip footing, which was later shown to be an exact solution satisfying upper and lower bound theorems of plasticity theory (Drucker et al. 1952). This basic solution is then modified using empirical or semi-empirical correction factors in order to account for the embedment depth, foundation shape, load inclination, eccentricity, etc. [after Meyerhof (1953); Brinch Hansen (1970); Vesic (1975)]. The accuracy of these correction factors is of particular interest for structures that are subject to large lateral and moment loading, including offshore breakwaters (Sekiguchi and Ohmaki 1992), gravity base platforms (Janbu 1985; Andersen and Lauritzen 1988; Bransby and Randolph 1997), and spud-can foundations for jack-up rigs (Houlsby and Martin 1992; Gottardi and Butterfield 1993; Dean et al. 1992; Murff 1994). Much of this recent research has focused on the development of more reliable failure criteria for shallow foundations under combined vertical, horizontal, and moment loading (V, H, M; Fig. 1), based either on direct experimental measurements (1g and centrifuge models), or computed by non-linear finite element analyses or approximate limit equilibrium methods.

The present paper applies techniques of numerical (upper and lower bound) limit analyses to establish the generalized, undrained failure criterion for combined loading of a surface strip footing. Rigorous upper and lower bound failure loads are solved by linear programming methods, while spatial discretization and interpolation of the field variables are accomplished using finite element methods. This approach combines the advantages of finite element methods for handling complex geometric and loading conditions, with the power of the limit theorems for bounding the exact collapse load. Although these techniques were first proposed by Lysmer (1970) and Bottero et al. (1980), their subsequent development was hampered by the excessive computation times required to solve large systems of sparse linear equations (originally carried out using simplex or revised simplex algorithms). This efficiency problem was resolved by Sloan (1988b) using a steepest edge active set algorithm (Best and Ritter 1985) that has now been implemented in both lower bound (Sloan 1988a) and upper bound (Sloan and Kleeman 1995) formulations. Full details on the numerical algorithms are given in these source papers, while Assadi and Sloan (1991) have demonstrated the application of these analyses for undrained stability of shallow tunnels. This paper gives a very brief summary of the two formulations, emphasizing only those aspects of the analyses that were developed for the current study of surface foundations.

Fig. 1 summarizes the problem notation. Combined loading of a footing of width, B, can be represented either by a resultant force, Q, at eccentricity, e, and inclination angle, α, or by three statically equivalent forces V, H, and M [Fig. 1(c)]. Loading conditions where Q is directed toward the centerline, Mode I ["backward eccentricity," Fig. 1(a)], can also be distinguished from Mode II conditions ["forward eccentricity," Fig. 1(b)] where the resultant force acts toward the edge of the footing. These modes correspond to different combinations of horizontal and moment loading [M-H plane, Fig. 1(d)]. For notation purposes, the horizontal load component always points toward the "leading edge" and away from the "trailing edge" of the footing.

The two most commonly used calculations to compute the

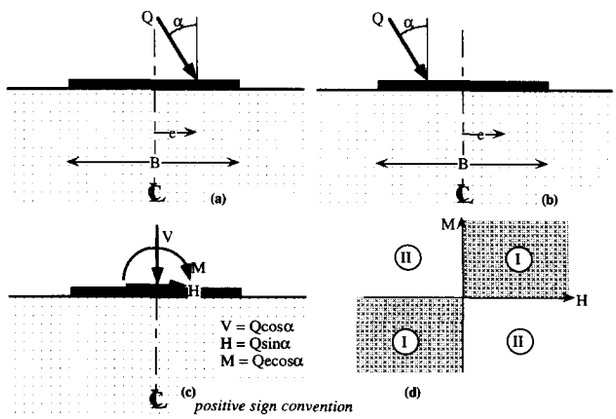

FIG. 1. Problem Notation: (a) Mode I; (b) Mode II; (c) Equivalent Forces; (d) Modes of Loading

[1]Grad. Res. Fellow, Dept. of Civ. and Envir. Engrg., Massachusetts Inst. of Technol., Cambridge, MA 02139.

[2]Assoc. Prof., Dept. of Civ. and Envir. Engrg., Massachusetts Inst. of Technol., Cambridge, MA.

[3]Assoc. Prof., Dept. of Civ. Engrg. and Surv., Univ. of Newcastle, Newcastle, NSW2308, Australia.

Note. Discussion open until August 1, 1998. To extend the closing date one month, a written request must be filed with the ASCE Manager of Journals. The manuscript for this paper was submitted for review and possible publication on April 16, 1997. This paper is part of the ***Journal of Geotechnical and Geoenvironmental Engineering***, Vol. 124, No. 3, March, 1998. ©ASCE, ISSN 1090-0241/98/0003-0265–0276/$4.00 + $.50 per page. Paper No. 15586.

maximum value of Q for combined loading of a surface strip footing on level ground are as follows:

for $\alpha \leq \alpha_0$:

$$\frac{Q}{Bs_u} = N_{c0}\left(1 - \frac{2e}{B}\right)\left[\frac{1}{\cos\alpha}\left(1 - \frac{\alpha^\circ}{90}\right)^2\right] \quad \text{Meyerhof (1953)} \quad (1a)$$

$$\frac{Q}{Bs_u} = N_{c0}\left(1 - \frac{2e}{B}\right)\left(\frac{1}{\cos\alpha + 2\sin\alpha}\right) \quad \text{Vesic (1975)} \quad (1b)$$

for $\alpha > \alpha_0$:

$$\frac{Q}{Bs_u} = \left(1 - \frac{2e}{B}\right)\frac{1}{\sin\alpha} \quad \text{Interface Sliding} \quad (1c)$$

where s_u = undrained, plane strain shear strength of (homogeneous) clay layer; N_{c0} = theoretical bearing capacity factor for vertical loading [for homogeneous clay, $N_{c0} = (2 + \pi)$, while analytical solutions for nonhomogeneous layers are given by Davis and Booker (1973)]; and α_0 = inclination angle at which undrained strength is mobilized at all points along horizontal soil-footing interface [$\alpha_0 = 15.99°$ and $17.59°$ in (1*a*) and (1*b*), respectively].

Both methods compute the capacity under combined loading as the product of two terms representing the effects of load eccentricity and inclination. For eccentric loading, the calculations assume a reduced area of contact between the soil and foundation, corresponding to the effective width, $B' = B - 2e$ (Meyerhof 1953), where it is implicitly assumed that $e > 0$. Hence, (1*a*) and (1*b*) do not recognize differences in capacity between combined loading in Modes I and II.

NUMERICAL LIMIT ANALYSES

Lower Bound Formulation

The lower bound theorem states that any *statically admissible stress* field will provide a lower bound (or "safe") estimate of the exact limit load. A statically admissible stress field is one which satisfies the equilibrium equations and stress boundary conditions, and must not violate the yield criterion of the material.

The numerical implementation of the lower bound analysis for plane strain problems discretizes the soil mass into three-noded triangular elements and assumes a linear variation of the unknown stresses (σ_x, σ_y, τ_{xy}) within each element (Fig. 2)

$$\sigma_x = \sum_{i=1}^{3} N_i\sigma_{xi}; \quad \sigma_y = \sum_{i=1}^{3} N_i\sigma_{yi}; \quad \tau_{xy} = \sum_{i=1}^{3} N_i\tau_{xyi} \quad (2)$$

where N_i = standard linear shape functions [e.g., Zienkiewicz (1983)]; and (σ_{xi}, σ_{yi}, τ_{xyi}) = stresses at node i.

In contrast to conventional displacement based finite element methods, each node is unique to a particular element such that stress discontinuities can occur along shared edges between elements (defined by pairs of nodes, e.g., 2, 4 and 3, 6, Fig. 2). The conditions of static admissibility are then derived as a series of linear constraints on the nodal stresses.

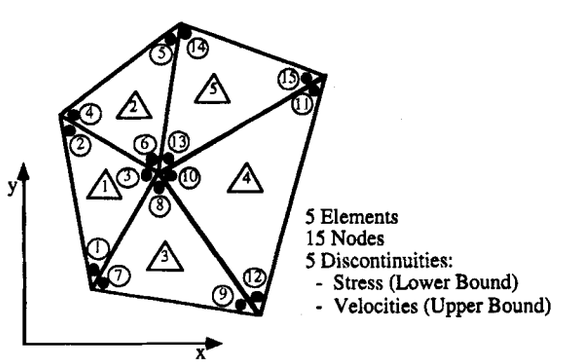

FIG. 2. Finite Element Discretization of Soil Mass

For plane strain analyses, the lower bound stress field must satisfy the following equations of equilibrium:

$$\frac{\partial\sigma_x}{\partial x} + \frac{\partial\tau_{xy}}{\partial y} = 0; \quad \frac{\partial\tau_{xy}}{\partial x} + \frac{\partial\sigma_y}{\partial y} = \gamma \quad (3)$$

where γ = unit weight of soil; and compressive stresses are positive.

Equilibrium of the nodal point stresses is then achieved by differentiating (2) and substituting into (3), generating a set of linear equalities in the form

$$\mathbf{A}_1\boldsymbol{\sigma}_1 = \mathbf{B}_1 \quad (4)$$

where $\boldsymbol{\sigma}_1$ = vector of nodal point stresses for each element

The shear and normal tractions must also be in equilibrium at all points along the discontinuities between elements. This condition can be satisfied by matching traction components at the nodal pairs (e.g., 2, 4 and 3, 6 in Fig. 2; and 1, a etc., for the soil-footing interface in Fig. 3)

$$\sigma_{n2} = \sigma_{n4} \quad \text{and} \quad \tau_2 = \tau_4 \quad (5a)$$

$$\sigma_{n3} = \sigma_{n6} \quad \text{and} \quad \tau_3 = \tau_6 \quad (5b)$$

For each interface, these relations can be rewritten as a series of equality constraints on the nodal point stresses by introducing standard transformation equations between surface tractions (σ_n, τ) and Cartesian stress components (σ_x, σ_y, τ_{xy})

$$\mathbf{A}_2\boldsymbol{\sigma}_2 = \mathbf{B}_2 \quad (6)$$

where $\boldsymbol{\sigma}_2$ = vector of nodal point stresses for two pairs of nodes at either end of discontinuity.

These same types of constraint can be used to represent all stress controlled boundary conditions.

The present analyses assume that the undrained shear strength of the clay can be represented by the isotropic Tresca yield criterion. Hence, for plane strain problems, the locus of admissible stress states can be written as

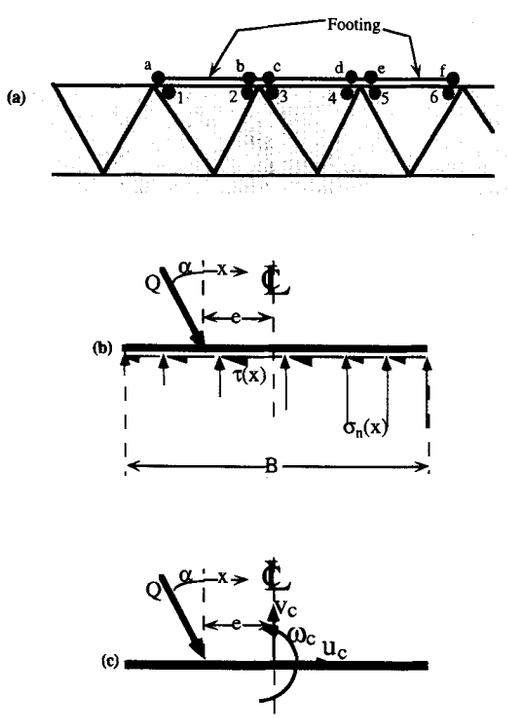

FIG. 3. Representation of Rigid Footing in Limit Analysis: (a) Representation; (b) Equilibrium of Footing; (c) Kinematics of Rigid Footing

$$F = X^2 + Y^2 - R^2 \leq 0 \tag{7}$$

where $X = (\sigma_y - \sigma_x)$ and $Y = 2\tau_{xy}$ = transformed stress components, defined such that the Tresca yield criterion ($F = 0$) plots as circular surface with radius $R = 2s_u$ (Fig. 4).

Following Lysmer (1970), this single nonlinear function can be approximated by an interior polygon, with p sides of equal length (Fig. 4). The locus of statically admissible stress states must then satisfy a series of linear inequality constraints of the form

$$F_k = A_k\sigma_x + B_k\sigma_y + C_k\tau_{xy} - D \leq 0 \tag{8}$$

where $k = 1 \cdots p$; linear coefficients A_k, B_k, and C_k are defined from the verticies of the polygon; and $D = 2s_u \cos(\pi/p)$.

As the stresses vary linearly within the element, the yield condition can be satisfied by enforcing a series of linear inequality constraints on the nodal point stresses, $F_{ki} \leq 0$, where F_{ki} is the kth side of the linearized yield function at node i. Thus, the linearized yield surface introduces p constraints on the stresses at each nodal point, written in matrix form as

$$\mathbf{A}_3\boldsymbol{\sigma}_3 \leq \mathbf{B}_3 \tag{9}$$

where $\boldsymbol{\sigma}_3$ = vector of stress components at each node in the mesh.

It should be noted that the analyses can be readily modified to simulate foundations that have no uplift capacity by truncating the yield function using a no-tension cutoff criterion (Fig. 5).

Finally, the vertical, horizontal, and moment equilibriums for the footing itself impose two additional constraints on the interface tractions [Fig. 3(b)]

$$\sin\alpha \int_s \sigma_n\, dx - \cos\alpha \int_s \tau\, dx = 0 \tag{10a}$$

$$\int_s x\sigma_n\, dx = 0 \tag{10b}$$

where x = distance measured from the point of the resultant load application (Fig. 3). As the stresses vary linearly across each element, the integrals in (10*a*) and (10*b*) can also be assembled in matrix form

$$\mathbf{A}_4\boldsymbol{\sigma}_4 = \mathbf{B}_4 \tag{11}$$

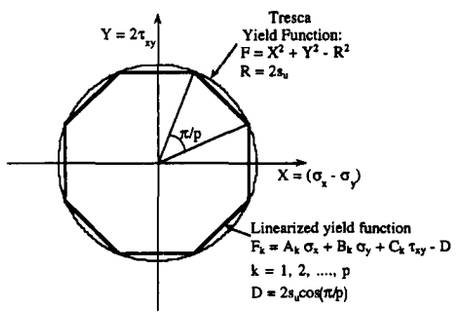

FIG. 4. Polygonal Representation of Tresca Yield Criterion for Lower Bound Analysis (after Sloan 1988b)

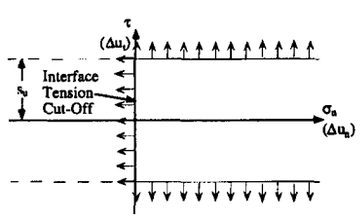

FIG. 5. Yield and Flow Directions for Soil-Footing Interface with Zero Underbase Suction

TABLE 1. Solution of Limit Analyses as Linear Programming Problems

Lower bound min $\{-\mathbf{C}^T\boldsymbol{\Sigma}\}$ (1)	Upper bound min $\{\mathbf{C}_2^T\boldsymbol{\Lambda} + \mathbf{C}_3^T\mathbf{U}^{\pm}\}$ (2)
(*a*) Subject To	
$\mathbf{A}_1\boldsymbol{\Sigma}_1 = \mathbf{B}_1$ $\mathbf{A}_2\boldsymbol{\Sigma}_2 = \mathbf{B}_2$ $\mathbf{A}_3\boldsymbol{\Sigma}_3 \leq \mathbf{B}_3$ $\mathbf{A}_4\boldsymbol{\Sigma}_4 = \mathbf{B}_4$ —	$\mathbf{A}_{11}\mathbf{U}_1 + \mathbf{A}_{12}\boldsymbol{\Lambda} = 0$ $\mathbf{A}_{21}\mathbf{U}_2 + \mathbf{A}_{22}\mathbf{U}^{\pm} = 0$ $\mathbf{A}_{31}\mathbf{U}_1 = \mathbf{B}_3$ $\boldsymbol{\Lambda} \geq 0$ $\mathbf{U}^{\pm} \geq 0$
(*b*) Where	
$\boldsymbol{\Sigma}$ is the global vector of nodal stresses	$\mathbf{U}_1$, $\boldsymbol{\Lambda}$, and $\mathbf{U}^{\pm}$ are global vectors of nodal velocities, plastic multipliers, and subsidiary tangential velocity jumps

where $\boldsymbol{\sigma}_4$ = vector of stresses at nodes along the soil-footing interface.

Eqs. (4), (6), (9), and (11) summarize the constraints on the nodal point stresses that ensure static admissibility. Lower bound estimates of the collapse load for surface footings are then obtained by maximizing the resultant force, Q (per unit width)

$$\max\{Q\} = \max\left\{\frac{1}{\cos\alpha}\int_s \sigma_n\, dx\right\} \tag{12}$$

Using the stress transformation relations, this objective function can be written as

$$\max \mathbf{C}^T\boldsymbol{\sigma} \quad \text{or} \quad \min -\mathbf{C}^T\boldsymbol{\sigma} \tag{13}$$

Hence, by assembling the coefficients for the complete finite element mesh, the lower bound analysis can be formulated as a linear programming problem that can be solved efficiently by an active set algorithm (Table 1; Sloan 1988b).

Upper Bound Formulation

An upper bound on the exact collapse load can be obtained by equating the power dissipated in *a kinematically admissible velocity field* with the power expended by the external loads (Drucker et al. 1952). A kinematically admissible velocity field is one that satisfies the compatibility equations, velocity boundary conditions, and the flow rule. During plastic flow, power is dissipated by plastic yielding of the soil mass, and by sliding along velocity discontinuities, where jumps in the normal and tangential velocities can occur.

The upper bound analysis for plane strain problems is solved numerically using three-noded triangular finite elements. Velocity discontinuities can occur along shared edges between elements, while the unknown soil velocities (u_x, u_y) vary linearly within each element

$$u = \sum_{i=1}^{3} N_i u_i; \quad v = \sum_{i=1}^{3} N_i v_i \tag{14}$$

where (u_i, v_i) = components of nodal point velocities; and N_i = linear shape functions.

In order to satisfy the conditions of kinematic admissibility, the plastic strain rates within each element must be compatible with the velocity field and satisfy the associated flow rule

$$\dot{\varepsilon}_x = -\frac{\partial u}{\partial x} = \dot{\lambda}\frac{\partial F}{\partial \sigma_x}; \quad \dot{\varepsilon}_y = -\frac{\partial v}{\partial y} = \dot{\lambda}\frac{\partial F}{\partial \sigma_y};$$

$$\dot{\gamma}_{xy} = -\left(\frac{\partial u}{\partial y} + \frac{\partial v}{\partial x}\right) = \dot{\lambda}\frac{\partial F}{\partial \tau_{xy}} \tag{15}$$

where $\dot{\varepsilon}_x$, $\dot{\varepsilon}_y$, $\dot{\gamma}_{xy}$ = plastic strain rates (positive in compression); $\dot{\lambda}$ = plastic multiplier; and F = (Tresca) yield function of clay.

For the upper bound calculation, the Tresca yield surface is represented by a p-sided polygon that externally circumscribes the exact function [(8) with $D = 2s_u$]. Hence, the conditions for a kinematically admissible velocity field within each element can be expressed as a series of linear constraints on the nodal point velocities and unknown plastic multiplier rates (for each of the p sides of the yield polygon) by combining (14), (15), and (8)

$$\sum_{i=1}^{3} \frac{\partial N_i}{\partial x} u_i + \sum_{k=1}^{p} \dot{\lambda}_k A_k = 0; \quad \sum_{i=1}^{3} \frac{\partial N_i}{\partial y} v_i + \sum_{k=1}^{p} \dot{\lambda}_k B_k = 0 \qquad (16a)$$

$$\sum_{i=1}^{3} \frac{\partial N_i}{\partial x} v_i + \sum_{i=1}^{3} \frac{\partial N_i}{\partial y} u_i + \sum_{k=1}^{p} \dot{\lambda}_k C_k = 0 \qquad (16b)$$

where $\dot{\lambda}_k \geq 0$.

These relations can be rewritten in a compact matrix form as

$$\mathbf{A}_{11}\mathbf{u}_1 + \mathbf{A}_{12}\boldsymbol{\lambda} = 0 \qquad (17)$$

where $\mathbf{u}_1$ and $\boldsymbol{\lambda}$ = vector of nodal point velocities and plastic multipliers, respectively, for each element.

The upper bound formulation allows velocity discontinuities to occur along shared edges between elements. The discontinuity can be characterized by a jump in the normal and tangential velocity components (Δu, Δv) between pairs of nodes (i, j) (e.g., 2, 4 or 3, 6 in Fig. 2)

$$\Delta u_{ij} = (u_j - u_i)\cos\theta + (v_j - v_i)\sin\theta \qquad (18a)$$

$$\Delta v_{ij} = (u_i - u_j)\sin\theta + (v_j - v_i)\cos\theta \qquad (18b)$$

where θ describes the orientation of the discontinuity.

In order to maintain kinematic admissibility, the velocity jump must satisfy the flow rule. For the Tresca yield condition, this requires that plastic deformation occur at constant volume with no jump in the normal velocity component, i.e.,

$$\Delta v_{ij} = 0 \qquad (19)$$

There is no restriction on the sign of the tangential velocity jump. However, its value can be constrained according to the requirements of standard linear programming methods, by introducing two subsidiary nonnegative variables (Δu^+, Δu^-) such that

$$\Delta u_{ij} = u_{ij}^+ - u_{ij}^- \quad \text{subject to:} \quad u_{ij}^+ \geq 0; \quad u_{ij}^- \geq 0 \qquad (20)$$

Eqs. (18), (19), and (20) can be combined to form a series of linear constraints, written in matrix form as

$$\mathbf{A}_{21}\mathbf{u}_2 + \mathbf{A}_{22}\mathbf{u}^{\pm} = 0 \qquad (21)$$

where $\mathbf{u}_2$ = vector of nodal velocities for the matched pairs (e.g., 2, 4 and 3, 6 in Fig. 2); and $\mathbf{u}^{\pm}$ = vector of subsidiary variables ($u_{12}^{\pm}$, etc.).

The total internal power, W_i, can be computed by summing the dissipation that occurs due to plastic deformation within each of the soil elements and by shearing along the velocity discontinuities between elements. The components of internal power dissipation are as follows:

within each element:

$$W_c = \int_A (\sigma_x\dot{\varepsilon}_x + \sigma_y\dot{\varepsilon}_y + \tau_{xy}\dot{\gamma}_{xy})\, dA = 2\sum_{k=1}^{p} \dot{\lambda}_k \int_A s_u\, dA = C_2^T\boldsymbol{\lambda} \qquad (22a)$$

along each discontinuity:

$$W_d = \int_L s_u|\Delta u_t|\, dL = \int s_u(\Delta u_t^+ + \Delta u_t^-)\, dL = C_3^T u^{\pm} \qquad (22b)$$

The motions of a rigid footing under combined loading can be represented by two unknown velocities, u_c, v_c, and an angular rotation, ω_c, defined about a fixed reference point at the center of the base [Fig. 3(c)]. The external work done by the applied load is then

$$W_e = Q\{u_c \sin\alpha - v_c \cos\alpha + \omega_c e \cos\alpha\} \qquad (23a)$$

An upper bound on the true collapse load can then be obtained by equating the total internal power dissipation and the external work, W_e

$$Q\{u_c \sin\alpha - v_c \cos\alpha + w_c e \cos\alpha\} = W_i \qquad (23b)$$

Hence, the resultant force, Q, can be obtained from (23b) by constraining movements of the footing such that

$$u_c \sin\alpha - v_c \cos\alpha + \omega_c e \cos\alpha = 1 \qquad (24)$$

This result can be combined with other velocity boundary conditions to form a set of constraints on the nodal point velocities

$$\mathbf{A}_3\mathbf{u}_1 = \mathbf{B}_3 \qquad (25)$$

The objective function for these upper bound analyses seeks to minimize the external applied load (i.e., min $\{Q\}$), which is equivalent to minimizing the total rate of internal power dissipation, min $\{W_i\}$ [from (23b) and (24)].

Table 1 summarizes the formulation of the upper bound analysis in a standard linear programming form. Sloan and Kleeman (1995) give full details of the condensation of these equations into the canonical form used by the steepest edge active set algorithm.

TYPICAL RESULTS

One of the principal advantages of the numerical limit analyses is that the true collapse load is always bracketed by results from the upper and lower bound calculations. However, careful mesh refinement is essential in order to achieve numerically accurate solutions, where the error bounds on the exact load are within a prescribed tolerance, say ±5%. Fig. 6 shows typical finite element meshes used for computing the undrained stability of footings on clay [after Ukritchon (1996)]. The mesh for the lower bound analysis uses a high element density (mesh refinement) close to the stress singularities at the edges of the footing. Extension elements are introduced in order to ensure statically admissible solutions at all points in the deep clay layer (half-space). These elements

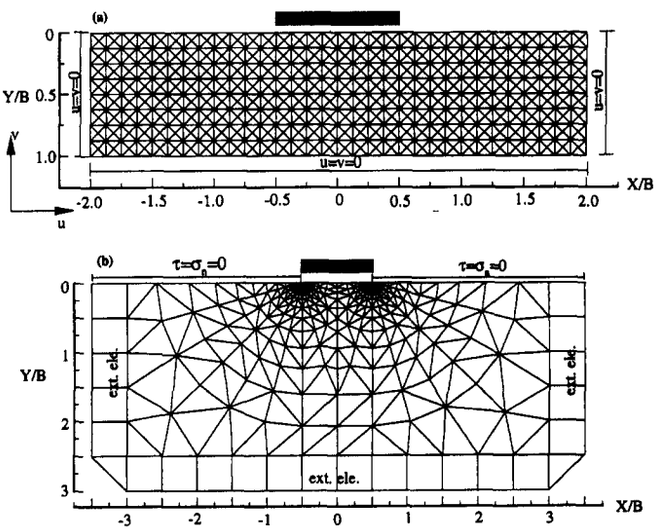

FIG. 6. Typical Finite Element Meshes Used for Numerical Limit Analyses: (a) Upper Bound Mesh; (b) Lower Bound Mesh

require special forms of the constraint equations for equilibrium and yield [cf., (4) and (9); Sloan (1988a)]. Most of the analyses reported in this paper consider that the base of the footing is rough (i.e., the interface shear traction, $|\tau| \leq s_u$), and assume there is either no tensile stress between the footing and soil ($\sigma_n \geq 0$; zero underbase suction) or that the normal stress is constrained only by the shear strength of the soil (full suction with no cavitation). Validation calculations for vertically loaded footings have also considered smooth bases ($\tau = 0$).

The mesh for the upper bound analysis is based on uniform squares, each subdivided into four triangular elements. There is apparently no advantage in more complex geometric arrangements, presumably due to the large number of velocity discontinuities permitted in the analysis. The size of the discretized domain must be sufficient to contain potential failure mechanisms, such that the far field boundaries can be represented as zero velocity conditions. Rigid body motions of the footing constrain the surface velocities at points along the interface. The analyses assume that separation can occur under combined loading if there is no suction at the interface. Fig. 5 shows how the flow directions are affected by the introduction of a tension cut-off in the yield criterion. This condition imposes the constraint that the normal velocity jump, $\Delta u_n \leq 0$, at points along the soil-footing interface.

Both upper and lower bound calculations assume a constant value, $p = 24$, for the yield surface linearization. Typical com-

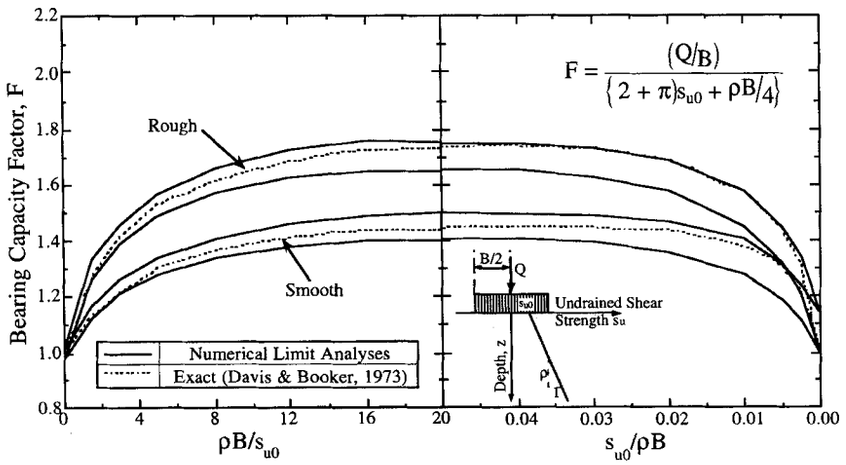

FIG. 7. Evaluation of Numerical Limit Analyses for Vertically Loaded Footings on Nonhomogeneous Clay Layers

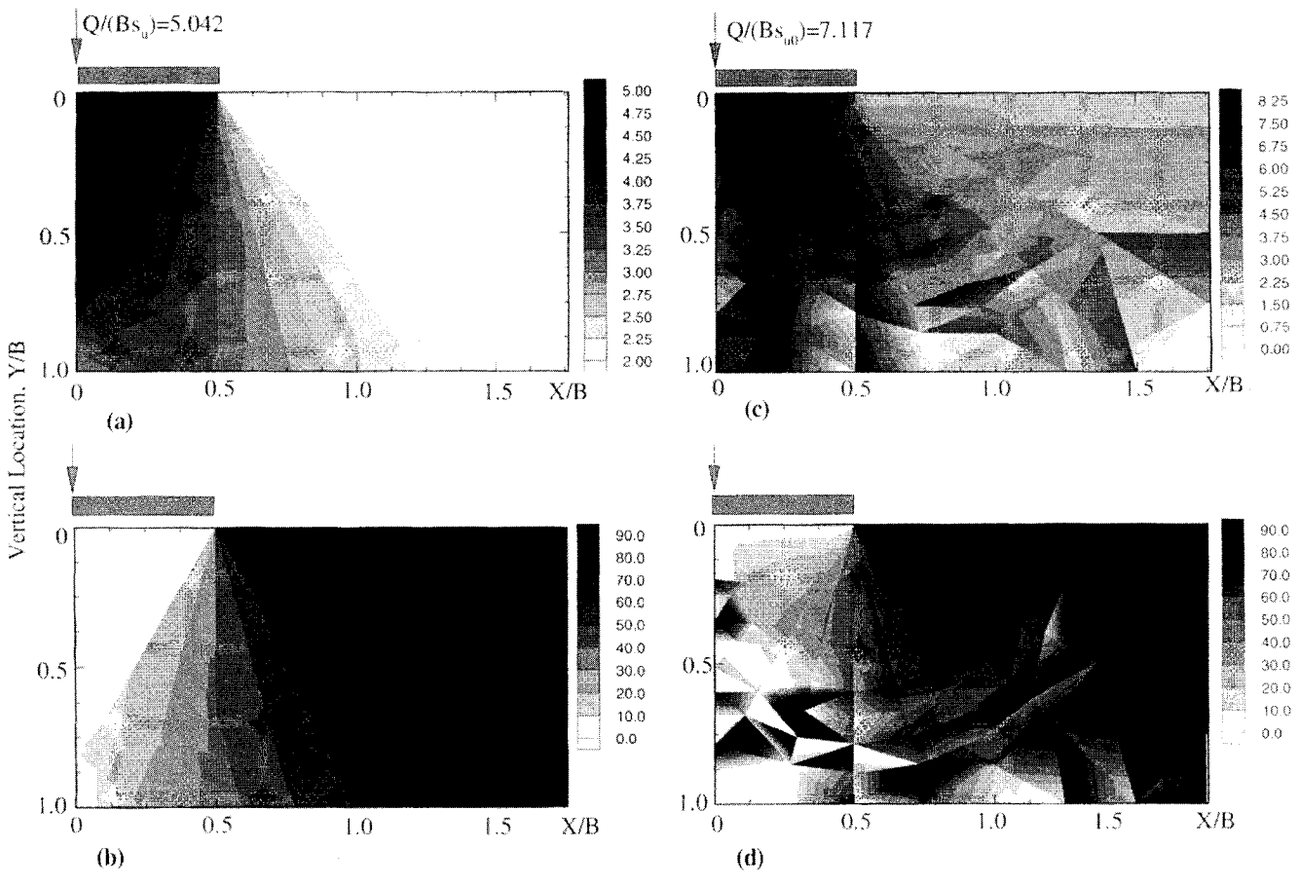

FIG. 8(a–d). Summary of Lower Bound Solutions for Vertically Loaded Footings (Smooth Base): (a) Contours of σ_1/s_u for $\rho B/s_u = 0$; (b) Orientation of σ_1 Relative to Vertical, δ, for $\rho B/s_u = 0$; (c) Contours of σ_1/s_u for $\rho B/s_{u0} = 3$; (d) Orientation of σ_1 Relative to Vertical, δ, for $\rho B/s_{u0} = 3$

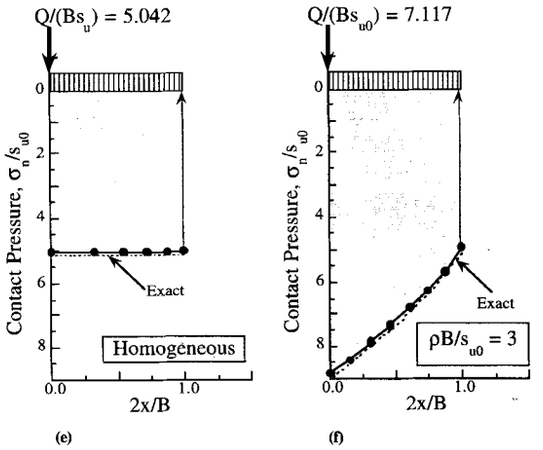

FIG. 8(e,f). Summary of Lower Bound Solutions for Vertically Loaded Footings (Smooth Base): (e) Contact Pressures, $\rho B/s_u = 0$; (f) Contact Pressures, $\rho B/s_{u0} = 3$

putation times for the analyses reported in the present paper range from 10–30 min of central processing unit on a DEC workstation (Alpha 3000-300x).

Fig. 7 summarizes the computed upper and lower bound estimates of the bearing capacity for vertically loaded footings on soil profiles where the undrained shear strength increases linearly with depth ($s_u = s_{u0} + \rho z$). The numerical solutions are compared with analytical results reported by Davis and Booker (1973) for smooth and rough bases. For the homogeneous case ($\rho B/s_{u0} = 0$), the interface shear strength has no effect on the bearing capacity, and the numerical solutions provide very tight bounds on the exact collapse load (3.7% difference between the upper and lower bound). For nonhomogeneous strength profiles with $\rho B/s_{u0} \leq 20$ the true collapse load is bounded within 5%–6%, and very good estimates of failure can be obtained by averaging the computed upper and lower bound loads [$Q_A = 1/2(Q_L + Q_U)$; the error on the exact load is then bounded within ±1.5%]. For small values of the ratio $s_{u0}/\rho B$ (0.005–0.05), the difference in computed bounds increases to 10%. Comparisons with the analytical solutions suggest that this range can be reduced by further mesh refinement for the lower bound calculation. In all cases, Q_A is within ±4.5% of the true collapse load. The mechanism of failure for $s_{u0}/\rho B = 0$ involves horizontal displacement of a surface veneer of soil beneath the footing, and cannot be simulated accurately by the numerical upper bound calculation.

Figs. 8(a–d) and 8(e,f) illustrate the character of the statically admissible stress fields by comparing lower bound predictions for smooth bases, and soil profiles with $\rho B/s_{u0} = 0$ and 3. As expected for the homogeneous case ($\rho B/s_{u0} = 0$), the major principal stress remains constant throughout a large zone of active shearing [$\delta = 0°$; Fig. 8(b)] beneath the footing. The region of principal stress rotation is well defined by a series of radial stress discontinuities [Fig. 8(a)], and passive shearing occurs in the surrounding soil [$\delta = 90°$; Fig. 8(b)]. The analysis predicts uniform vertical contact stresses across the width of the footing [Fig. 8(e)]. In contrast, lower bound calculations for $\rho B/s_{u0} = 3$ show that contact stresses increase toward the center of the footing [the results match analytical solutions from Davis and Booker (1973); Fig. 8(f)], while the zone of principal stress rotation extends to all points beneath the footing [Fig. 8(d)]. The results of upper bound analyses for the same two examples are shown in Fig. 9, and provide information on the location of the plastic zone and failure mechanisms [interpreted from velocity vectors, Figs. 9(b) and 9(d); and mesh deformations, Figs. 9(a) and 9(c)]. Although the results for the homogeneous case are very similar to the mechanism proposed by Prandtl, the numerical analyses predict some lateral spreading in the soil beneath the smooth base, and a slightly larger plastic failure zone. For the nonhomogeneous strength profile [$\rho B/s_{u0} = 3$; Figs. 9(c) and 9(d)], the plastic failure zone is greatly reduced in size, and the mechanism is dominated by lateral spreading toward the edge of the footing.

PREDICTIONS FOR COMBINED LOADING

Eccentric and Inclined Loading

Figs. 10 and 11 summarize the results of lower and upper bound analyses for footings on homogeneous soil with [part (a) depicting] vertical, eccentric loading ($H = 0$) and [part (b) depicting] inclined central loading ($M = 0$). These calculations all assume a rough interface with no underbase suction (i.e., tension cut-off is in effect; Fig. 5). Lower bound calculations confirm that the reduction in footing capacity for vertical eccentric loading [Fig. 10(a)] is related to the loss of contact pressure at the trailing edge of the footing. At an eccentricity $e/B = 0.25$, approximately 50% of the footing remains in contact with the soil. For inclined central loading, full mobilization of the horizontal shear resistance occurs at relatively small inclination angles [e.g., at $\alpha = 15°$, $\tau/s_u \geq 0.90$ over most of the footing; Fig. 10(b)]. The upper bound calculations for the same loading conditions [Fig. 11(a–c)] show clearly the transition in failure mechanisms from a vertically penetrating ac-

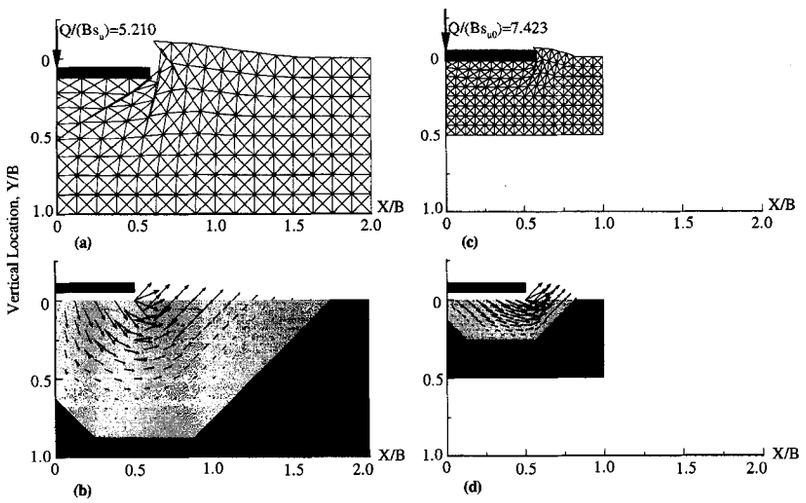

FIG. 9. Summary of Upper Bound Solutions for Vertically Loaded Footings with Smooth Base (Note: Light Shading—Plastic Zone): (a) Deformed Mesh, $\rho B/s_u = 0$; (b) Deformed Mesh, $\rho B/s_{u0} = 3$; (c) Failure Mechanism, $\rho B/s_u = 0$; (d) Failure Mechanism, $\rho B/s_{u0} = 3$

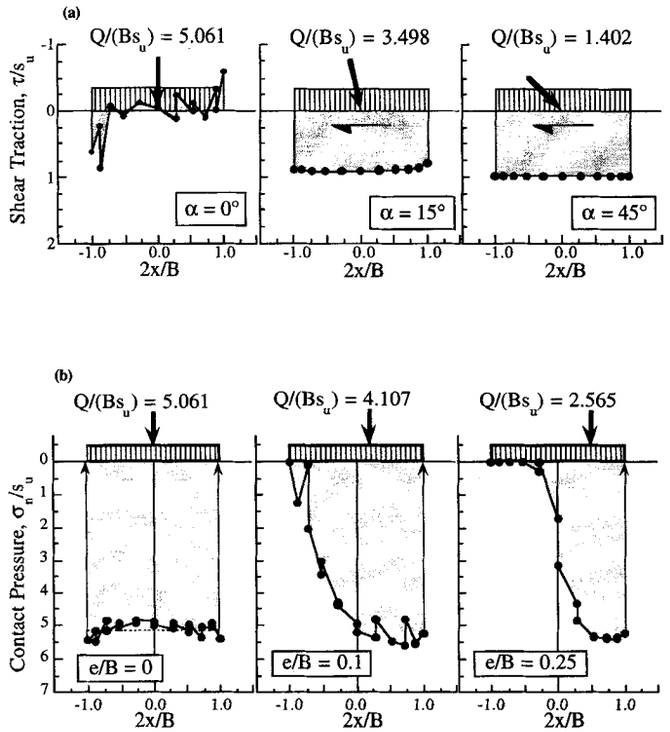

FIG. 10. Footing Interface Tractions from Lower Bound Analysis: (a) Vertical, Eccentric Loading; (b) Inclined, Central Loading

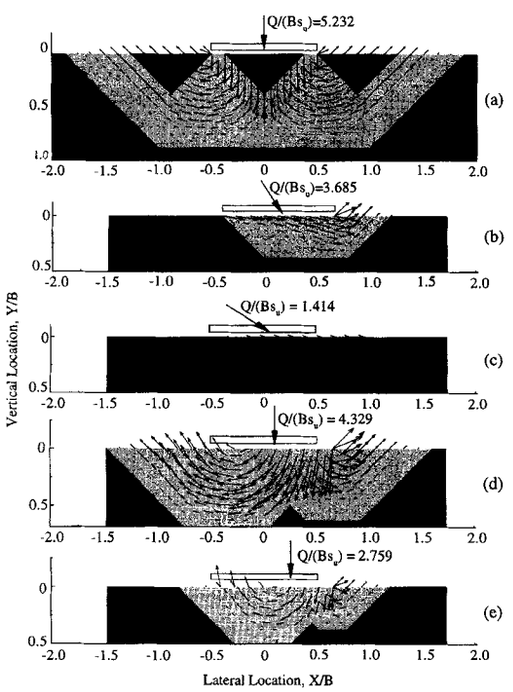

FIG. 11. Summary of Upper Bound Mechanisms for Vertical, Eccentric and Inclined, Central Loading: (a) $\alpha = 0°$, $e/B = 0$; (b) $\alpha = 15°$, $e/B = 0$; (c) $\alpha = 45°$, $e/B = 0$; (d) $\alpha = 0°$, $e/B = 0.10$; (e) $\alpha = 0°$, $e/B = 0.25$

tive wedge at $\alpha = 0°$, to a sliding wedge at $\alpha = 15°$ and full interface sliding at $\alpha = 45°$. As the eccentricity of the applied vertical load increases [$e/B = 0$, 0.1, 0.25; Figs. 11(a), 11(d), 11(e)], there is an overall reduction in the volume of the failure zone. At the leading edge of the footing, the mechanism of failure closely resembles the sliding wedge from Fig. 11(b). The pivot point for rotation is located close to the ground surface and migrates toward the centerline as the load eccentricity increases. At $e/B = 0.25$, separation occurs at the trailing edge of the footing (for $x/B < 0.15$) and the rotational mechanism is fully contained beneath the base (note that the onset of separation occurs at $e/B = 0.20$).

Combined Loading

The preceding upper and lower bound calculations have been extended for selected combinations of inclination angle, $\alpha = 0°–90°$, and eccentricity, $-0.35 \leq e/B \leq 0.35$. Fig. 12 shows the computed collapse loads as contour lines, corresponding to constant values of α and e/B, projected in two orthogonal planes [$V/(Bs_u)$, $M/(B^2 s_u)$] and [$V/(Bs_u)$, $H/(Bs_u)$]. In all cases, the upper and lower bound calculations are able to estimate the true collapse load within ±4%–5%. More precise bounds (±0.5%) occur for cases dominated by interface sliding, where $|H/(Bs_u)| \rightarrow 1$ [Fig. 12(b)]. The maximum moment for both loading modes can be well estimated by $|M/(B^2 s_u)| = N_{c0}/8 = 0.643$ [at $V/(Bs_u) = N_{c0}/2$, where $N_{c0} = (2 + \pi)$], as predicted using the effective width concept of Meyerhof (1953). The reduction in moment capacity for values of $V/$

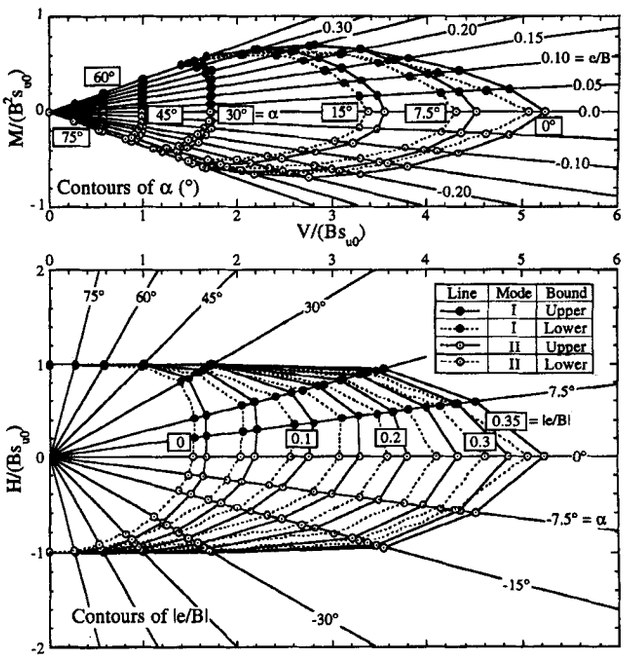

FIG. 12. Projections of Failure Surface for Combined Loading of Footing on Homogeneous Clay

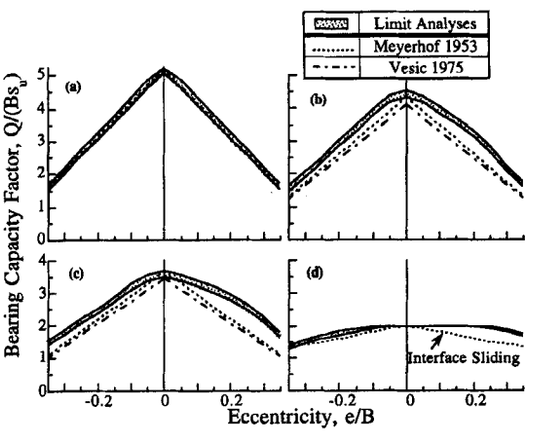

FIG. 13. Evaluation of Empirical Bearing Capacity Factors for Combined Loading on Homogeneous Clay: (a) $\alpha = 0°$; (b) $\alpha = 7.5°$; (c) $\alpha = 15°$; (d) $\alpha = 30°$

$(Bs_u) < 2.0-3.0$ is caused by the assumption that there is no underbase suction, and, hence, the area of contact between the footing and soil reduces to zero as $|e/B| \rightarrow 0.5$. The effects of eccentricity mode (I versus II) can be seen from the lack of symmetry of the projected contour lines in Figs. 12(a) and 12(b). The most pronounced differences occur for $e/B > 0.25$, and $\alpha = 15°-30°$, where footing capacity in Mode II loading is up to 20%–25% less than that in Mode I.

Fig. 13 compares the predicted limit loads $[Q/(Bs_u)]$ with conventional bearing capacity calculations using the empirical correction factors given in (1). In general, the empirical calculations are conservative and underestimate the limit loads for combined loading by up to 25%. More detailed observations show that (a) the concept of effective width matches the lower bound solutions for vertical eccentric loading [$\alpha = 0°$, Fig. 13(a)]; and (b) the empirical inclination factors proposed by Meyerhof (1953) are in better agreement with predicted limit loads for inclined central loading ($e/B = 0$) than those introduced by Vesic (1975).

Effects of Underbase Suction

For certain types of offshore foundation, such as gravity bases with short skirt piles, underbase suction can contribute significantly to the short-term undrained stability. Figs. 14(a) and 14(b) compare three-dimensional failure envelopes (defined in terms of the statically equivalent loads V, H, and M) for footings with zero underbase suction (derived from Fig. 13) and with full suction. In this representation, it is convenient to report the best estimate of the true collapse load as the average of the upper and lower bound predictions. Underbase suction preserves the moment capacity of the footing at low vertical load ratios, V/V_0 (where the maximum vertical capacity, $V_0 = N_{c0}s_u$), but has no effect on the predicted failure conditions for $V/V_0 > 0.65$.

Differences between Mode I and Mode II loading can be seen most clearly in cross sections of the failure surfaces at constant values of V/V_0 (H-M planes), Fig. 15. For both modes of loading, the maximum horizontal load capacity is con-

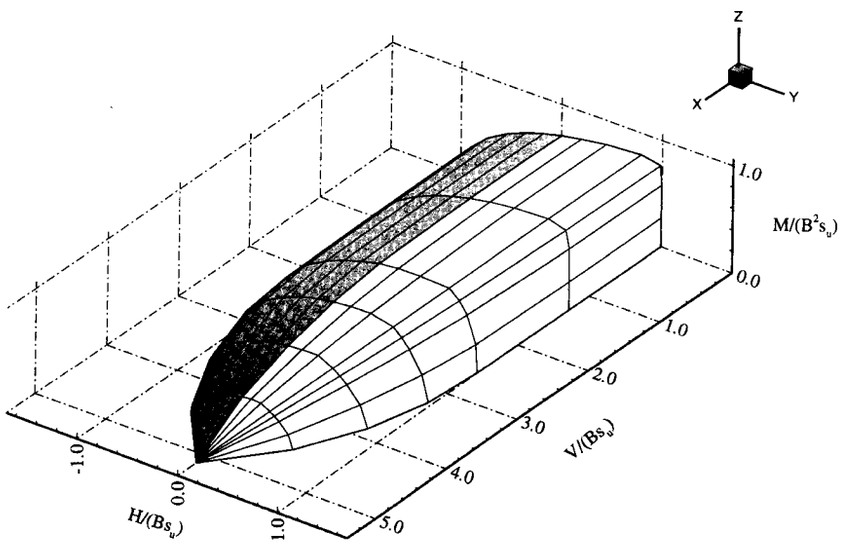

FIG. 14(a). Three-Dimensional Failure Envelopes for Footings on Homogeneous Clay—Full Underbase Suction

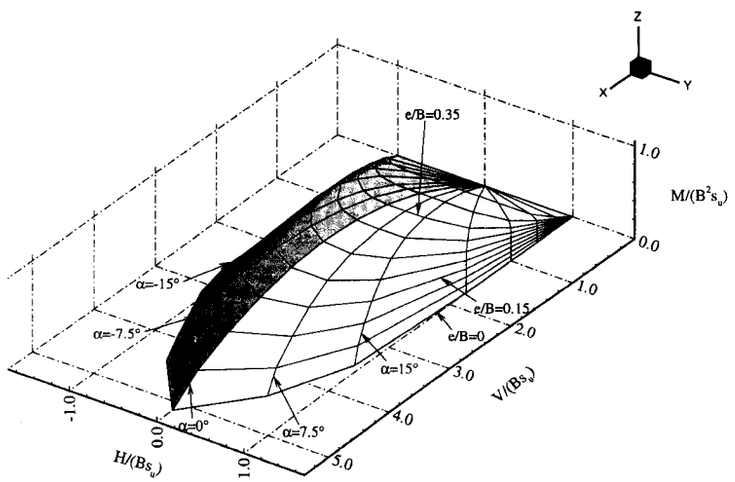

FIG. 14(b). Three-Dimensional Failure Envelopes for Footings on Homogeneous Clay—Zero Underbase Suction

strained by $H/Bs_u \leq 1.0$. At large vertical load ratios, $V/V_0 > 0.875$, the maximum moment capacity occurs when $H/Bs_u = 0$ and the failure locus is approximately symmetric. As the vertical load ratio decreases from $V/V_0 = 0.825$ to 0.5, the failure surface becomes increasingly skewed with the maximum moment capacity occurring for mode I combinations of H and M. For $V/V_0 < 0.5$, the vertical load has minimal effect on Mode II failure conditions (with full suction), while Mode I produces a maximum moment capacity, $M/(B^2s_u) = 0.8$ [at $H/(Bs_u) \approx 0.8$] for $V/V_0 \leq 0.25$. At these same sections, the failure envelope for Mode I loading is truncated by the constraint of maximum horizontal load capacity.

Figs. 16 and 17 present more detailed results of the upper and lower bound analyses, respectively, for three loading conditions labeled A, B, and C in Fig. 15 [all at $V/V_0 = 0.5$, with $|H/(Bs_u)| = 0.7$; i.e., $\alpha = 55°$]. The comparisons between A and B show the role of underbase suction in Mode I, while the results for C are typical of Mode II combined loading (and are not affected by the underbase suction). There is a large reduction in the interface contact area for case A [zero suction, Fig. 16(a)]. The failure mechanism can be characterized by an active zone that rotates about a pivot point located below the detachment point on the base of the footing (at $x/B \approx -0.125$, $y/B \approx 0.5$), connecting to a rotational shear zone and a passive wedge. Very similar failure mechanisms have been assumed in upper bound analyses by Salencon and Pecker (1995a,b) and in limit equilibrium calculations (Lauritzen and Schjetne 1976). The lower bound calculations [Fig. 16(a)] show that the maximum vertical bearing pressures ($N_{c0}s_u$) are mobilized at the leading edge of the footing, while shear tractions are fully mobilized from the trailing edge to the centerline.

With full underbase suction [case B, Fig. 16(b)] there is a rotational failure mechanism contained beneath the base of the footing (centered close to the ground surface and slightly offset from the centerline), and a failure wedge at the leading edge of the footing [this is similar to the scoop-wedge mechanism proposed by Bransby and Randolph (1997)]. The lower bound calculations predict that tensile stresses occur toward the trailing edge of the footing ($x/B < -0.6$); however, underbase suction has little effect on the distribution of the shear tractions [τ/s_u, Figs. 16(b) and 16(a)]. Failure in Mode II involves a single scoop mechanism extending slightly beyond the leading edge of the footing. The normal stress varies linearly across the base from a maximum bearing pressure at the trailing edge to zero at the leading edge of the footing (hence, the direction of the major principal stress also varies from $\delta = 0°-45°$).

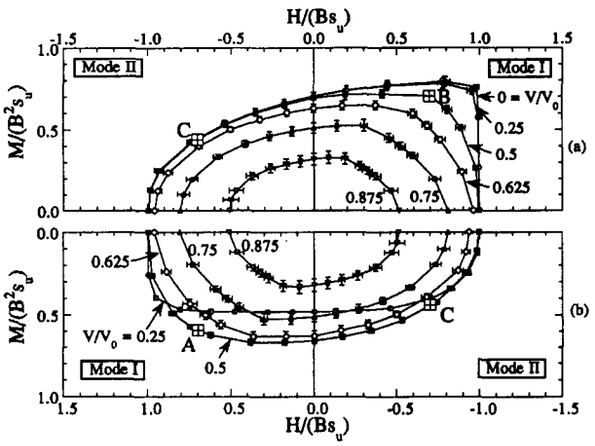

FIG. 15. Cross Sections of Failure Envelopes for Footings on Homogeneous Clay: (a) Full Base Suction; (b) Zero Base Suction

Effect of Non-Homogeneous Strength Profile

Limit analyses have also been carried out for combined loading of nonhomogeneous clay profiles where the undrained shear strength increases linearly with depth for $0 \leq \rho B/s_{u0} \leq 12$ (cf., Fig. 2), assuming zero underbase suction. Figs. 18(a) and 18(b) summarize the results for cases of vertical, eccentric and inclined, central loading. As expected, the maximum

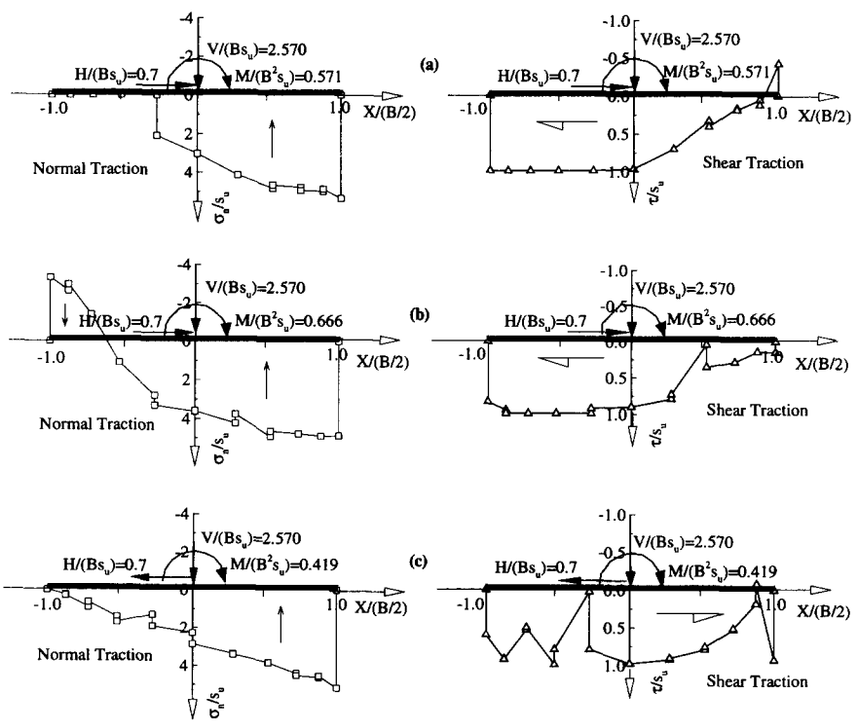

FIG. 16. Examples of Lower Bound Solutions for Combined Loading of Footings on Homogeneous Clay: (a) Zero Underbase Suction, Mode I; (b) Full Underbase Suction, Mode I; (c) Mode II

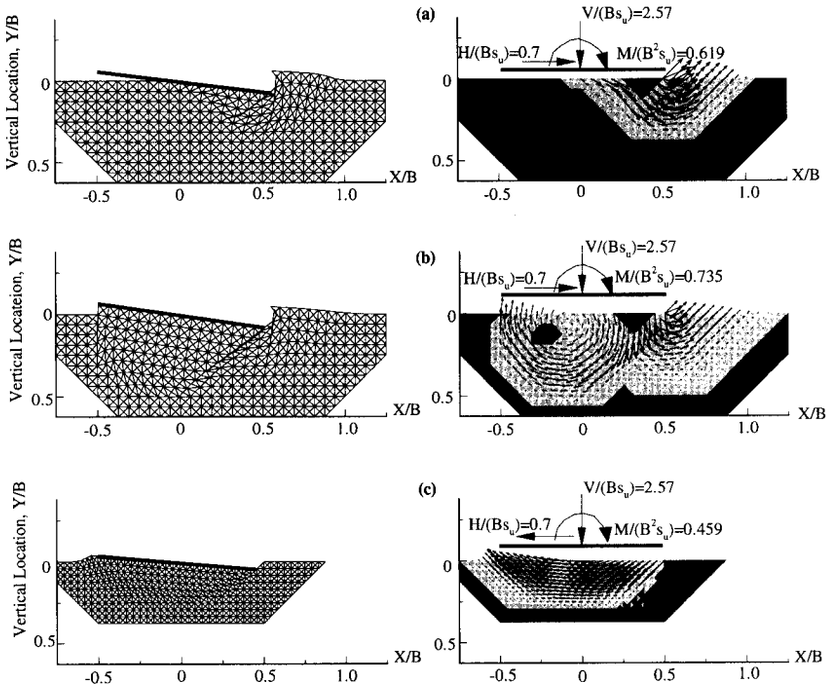

FIG. 17. Examples of Upper Bound Solutions for Combined Loading of Footings on Homogeneous Clay: (a) Zero Underbase Suction, Mode I; (b) Full Underbase Suction, Mode I; (c) Mode II

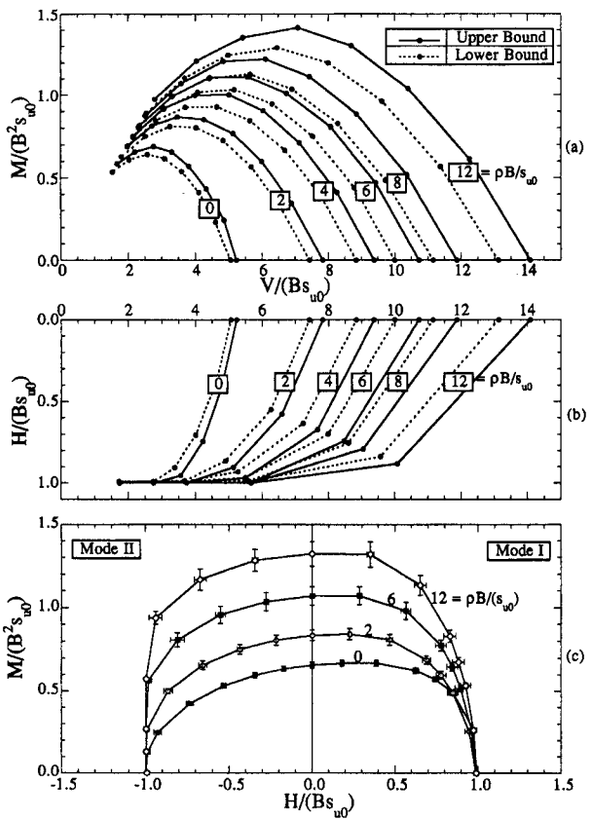

FIG. 18. Failure Envelopes for Footings on Clay Layers with Undrained Strength Gradient: (a) Vertical, Eccentric Loading; (b) Inclined, Central Loading; (c) Combined Loading at $V/V_0 = 0.5$ [Note: Exaggeration of Vertical Axes in (a) and (b)]

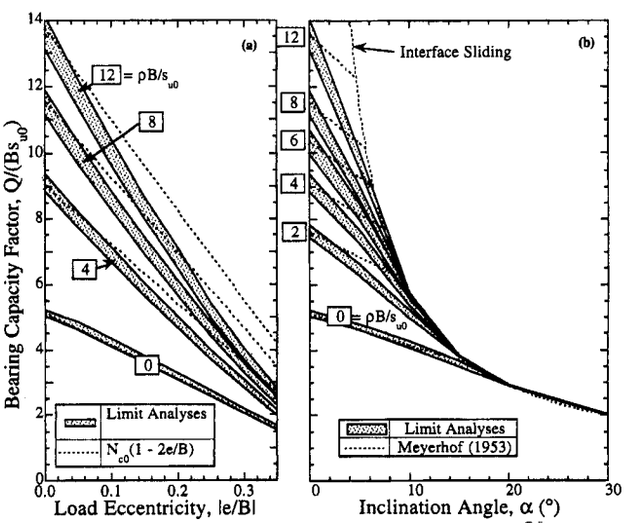

FIG. 19. Evaluation of Bearing Capacity Factors for Footings on Nonhomogeneous Clay Layers: (a) Vertical, Eccentric Loading; (b) Inclined, Central Loading

horizontal shear resistance is controlled by the strength of the surficial soil [$H/(Bs_{u0}) \leq 1$], while the maximum moment capacity occurs at a vertical load ratio, $V/V_0 = 0.5$, and ranges from $M/(B^2 s_{u0}) = 0.65$ to 1.35 for $\rho B/s_{u0} = 0$, 12, respectively.

Fig. 18(c) illustrates the effects of the undrained strength gradient on the shape of the yield envelope in the H-M plane at $V/V_0 = 0.5$. The yield surface remains non-symmetric as the profile parameter $\rho B/s_{u0}$ rises, while increases in the moment capacity are more pronounced for Mode II than for Mode I.

There are no published solutions specifically for combined loading of footings on nonhomogeneous clay layers. However, it is conventional practice [e.g., Det Norske Veritas (1992)] to apply the correction factors given in (1) together with analytical solutions for N_{c0} (Davis and Booker 1973). Fig. 19 compares the predicted limit loads with these empirical calculations. It is clear that the empirical calculations can greatly overestimate the actual limit load, especially at small inclination angles [$\alpha \leq 10°$; Fig. 19(b)], and/or large eccentricities [$|e/B| > 0.1$; Fig. 19(a)].

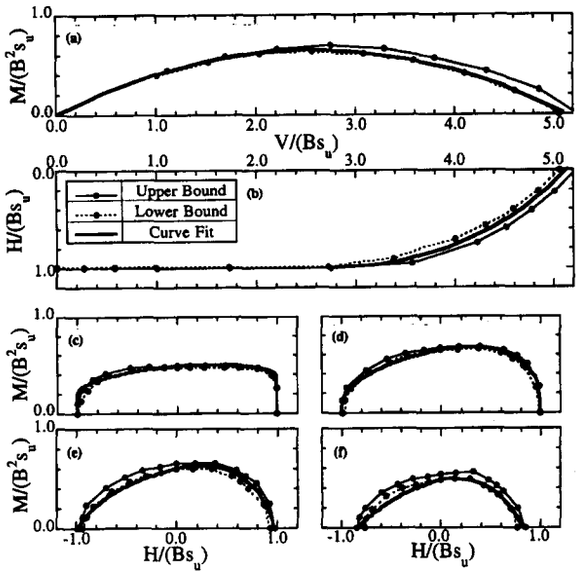

FIG. 20. Evaluation of Proposed Curve Fit for Combined Loading of Footings on Homogeneous Clay: (a) Vertical, Eccentric Loading; (b) Inclined, Central Loading; (c) Combined, V/V_0 = 0.25; (d) Combined, V/V_0 = 0.5; (e) Combined, V/V_0 = 0.625; (f) Combined, V/V_0 = 0.75

EMPIRICAL EQUATIONS FOR FAILURE ENVELOPE

The failure envelopes for combined loading have relatively complex geometries, which are most clearly illustrated by the *H-M* cross sections shown in Figs. 15 and 18(c). In part, this reflects the transition in failure mechanisms for different combinations of loading, underbase suction, undrained strength profiles, etc. Although undrained stability can be estimated directly from the results presented in this paper (or evaluated through further computation), it is more convenient if the solutions can be computed reliably using simple functions. Approximate empirical equations have been developed to describe the failure envelope for footings on homogeneous clay with zero underbase suction. The curve fitting procedure is based on a dimensional analysis which shows that

for $e/B \geq 0$

$$\tilde{V} = a_1 \left\{ 1 - a_2 \left(\frac{2e}{B} \right) - a_3 \left(\frac{2e}{B} \right)^2 \right\} \tag{26}$$

where $\tilde{V} = V/(Bs_u)$; eccentricity ratio $e/B = \tilde{M}/\tilde{V}$ [$\tilde{M} = M/(B^2 s_u)$]; and a_1, a_2, and a_3 = all functions of $\tilde{H} = H/(Bs_u)$. For inclined, central loading, (16) reduces to $\tilde{V} = a_1$.

The functions a_1, a_2, and a_3 are determined by empirical curve fitting of the numerical failure envelope

for $-1 \leq \tilde{H} \leq 1$:

$$a_1 = 1 + \pi - 0.8761 \sin^{-1}|\tilde{H}| + \sqrt{1 - \tilde{H}^2} \tag{27a}$$

Mode I, $0 \leq \tilde{H} \leq 1$:

$$a_2 = 1 - \tilde{H} + 0.8\tilde{H}^2; \quad a_3 = 1 - a_2 \tag{27b}$$

Mode II, $-1 \leq \tilde{H} \leq 0$:

$$a_2 = (2 + \pi)/a_1; \quad a_3 = 0 \tag{27c}$$

Fig. 20 compares the empirical equations with the numerically-derived failure envelope. For vertical eccentric loading, (26) is identical to the equation proposed by Meyerhof (1953) using the effective width concept, and matches closely with the lower bound limit analyses. For inclined central loading, the function a_1 (27*a*) is similar to an equation proposed by Bolton (1979) and corresponds to an average of the numerical bounds. Fig. 20 shows that (27*b*) gives an excellent match to the Mode I failure envelope, while (27*c*) gives a conservative estimate of the Mode II collapse loads (especially at high V/V_0).

The use of separate functions for Modes I and II [(27*b*) and (27*c*)] is a limitation of the present curve fitting solution. For example, the equations do not guarantee convexity of the failure envelope, and this may restrict the application of the empirical functions in further structural stability applications [cf., Murff (1994)].

CONCLUSIONS

The recent numerical formulation of upper and lower bound limit analyses, using finite element discretization and linear programming methods, provides a practical, efficient, and accurate method for estimating the undrained stability of foundations on clay. The exact failure conditions for combined loading of surface strip footings can be estimated within ±5% for all of the numerical limit analyses presented in this paper. The calculations for combined vertical, horizontal, and moment loading are summarized in the form of convex failure envelopes for homogeneous clays and profiles where the undrained shear strength increases linearly with depth. The results clarify differences in failure mechanisms between two modes of combined loading (Fig. 1), and identify the additional stability provided by underbase suction (which can be mobilized for offshore shallow foundations). Empirical bearing capacity correction factors (for load eccentricity and inclination) are conservative, and can underestimate the true combined collapse load on homogeneous clay by more than 20%. However, the same correction factors are completely unreliable (and non-conservative) for situations where there is an undrained strength gradient ($\rho B/s_{u0} > 0$). The undrained stability for combined loading of surface foundations can be either estimated directly from results presented in this paper or computed using the proposed curve fitting functions, based on dimensional analysis.

ACKNOWLEDGMENTS

The first writer is grateful to the Anada Mahidol Foundation, Thailand, for supporting his graduate studies at Massachusetts Institute of Technology. This paper was completed while the second writer was visiting the Geomechanics Group, University of Western Australia, supported by a Gledden Fellowship. Special thanks go to Fraser Bransby and Mark Randolph for their enlightening discussions on upper bound mechanisms. The upper and lower bound codes used in this paper were originally developed by the third writer with support from the Australian Research Council.

APPENDIX. REFERENCES

Andersen, K. H., and Lauritzen, R. (1988). "Bearing capacity for foundations with cyclic loads." *J. Geotech. Engrg.*, ASCE, 114(5), 540–555.

Assadi, A., and Sloan, S. W. (1991). "Undrained stability of shallow square tunnel." *J. Geotech. Engrg.*, ASCE, 117(8), 1152–1173.

Best, M. J., and Ritter, K. (1985). *Linear programming: Active set analysis and computer programs*. Prentice-Hall, Englewood Cliffs, N.J.

Bolton, M. D. (1979). *A guide to soil mechanics*. Macmillan, London.

Bottero, A., Negre, R., Pastor, J., and Turgeman, S. (1980). "Finite element method and limit analysis theory for soil mechanics problems." *Comp. Meth. Appl. Mech. Engrg.*, 22, 131–149.

Bransby, M. F., and Randolph, M. F. (1997). "Shallow foundations subject to combined loadings." *Proc., ISOPE'97*.

Brinch Hansen, J. (1970). "A revised and extended formula for bearing capacity." *DGI Bull. No. 28*, Danish Geotech. Inst., 5–11.

Davis, E. H., and Booker, J. R. (1973). "The effect of increasing strength with depth on the bearing capacity of clays." *Géotechnique*, 23(4), 551–563.

Dean, E. T. R., James, R. G., Schofield, A. N., Tan, F. S. C., and Tsu-

kamoto, Y. (1992). "The bearing capacity of conical footings on sand." *Predictive soil mechanics*. Thomas Telford, London, 230–253.
Det Norske Veritas. (1992). "Foundations." *Classification Notes No. 30.4*, Det Norske Veritas, Hovik, Norway.
Drucker, D. C., Greenberg, H. J., and Prager, W. (1952). "Extended limit design theorems for continuous media." *Q. Appl. Math.*, 9, 381–389.
Gottardi, G., and Butterfield, R. (1993). "On the bearing capacity of surface footings on sand under general planar loads." *Soils and Found.*, 33(3), 68–79.
Houlsby, G. T., and Martin, C. M. (1992). "Modelling on the behaviour of jack-up units on clay." *Predictive soil mechanics*. Thomas Telford, London, 339–358.
Janbu, N. (1985). "Soil models in offshore engineering." *Géotechnique*, 35(3), 239–283.
Lauritzen, R., and Schjetne, K. (1976). "Stability calculations for offshore gravity structures." *Proc., 8th Offshore Technol. Conf.*, Paper No. OTC 2431.
Lysmer, J. (1970). "Limit analysis of plane problems in soil mechanics." *J. Soil Mech. Found. Div.*, ASCE, 96(4), 1311–1334.
Meyerhof, G. G. (1953). "The bearing capacity of foundation under eccentric and inclined loads." *Proc., 3rd Int. Conf. on Soil Mech. and Found. Engrg.*, 1, 440–445.
Murff, J. D. (1994). "Limit analysis of multi-footing foundation systems." *Proc., 8th IACMAG*, 1, 233–244.
Prandtl, L. (1920). *Über die harte plastischer körper*. Nachr. K. Ges. Wiss. Gott., Math-Phys. Kl., 74–85.
Salencon, J., and Pecker, A. (1995a). "Ultimate bearing capacity of shallow foundations under inclined and eccentric loads. Part I: Purely cohesive soil." *Eur. J. Mech. A/Solids*, 14(3), 349–375.
Salencon, J., and Pecker, A. (1995b). "Ultimate bearing capacity of shallow foundations under inclined and eccentric loads. Part II: Purely cohesive soil without tensile strength." *Eur. J. Mech. A/Solids*, 14(3), 377–396.
Sekiguchi, H., and Ohmaki, S. (1992). "Overturning of caissons by storm wave." *Soils and Found.*, 32(3), 144–155.
Sloan, S. W. (1988a). "Lower bound limit analysis using finite elements and linear programming." *Int. J. Numer. Anal. Methods in Geomech.*, 12(1), 61–77.
Sloan, S. W. (1988b). "A steepest edge active set algorithm for solving sparse linear programming problems." *Int. J. Numer. Anal. Methods in Geomech.*, 26(12), 2671–2685.
Sloan, S. W., and Kleeman, P. W. (1995). "Upper bound limit analysis using discontinuous velocity fields." *Comp. Methods in Appl. Mech. and Engrg.*, 127, 293–314.
Terzaghi, K. (1943). *Theoretical soil mechanics*. John Wiley & Sons, Inc., New York, N.Y.
Ukritchon, B. (1996). "Evaluation of numerical limit analyses by finite elements and linear programming," MS thesis, Dept. of Civ. and Envir. Engrg., Massachusetts Inst. of Technol., Cambridge, Mass.
Vesic, A. S. (1975). "Bearing capacity of shallow foundations." *Foundation engineering handbook*, H. F. Winterkorn and H. Y. Fang, eds., Van Nostrand Reinhold, New York, N.Y., 121–145.
Zienkiewicz, O. C. (1983). *The finite element method*. McGraw-Hill Book Co., Inc., New York, N.Y.